Physics of Fluids

An enriched finite element/level-set model for two-phase electrohydrodynamic simulations

Cite as: Phys. Fluids **35**, 012004 (2023); https://doi.org/10.1063/5.0127274
Submitted: 20 September 2022 • Accepted: 08 December 2022 • Published Online: 04 January 2023

Christian Narváez-Muñoz, Mohammad R. Hashemi, Pavel B. Ryzhakov, et al.

Physics of Fluids ARTICLE scitation.org/journal/phf

An enriched finite element/level-set model for two-phase electrohydrodynamic simulations

Cite as: Phys. Fluids **35**, 012004 (2023); doi: 10.1063/5.0127274
Submitted: 20 September 2022 · Accepted: 8 December 2022 ·
Published Online: 4 January 2023

Christian Narváez-Muñoz,[1,2,a)] Mohammad R. Hashemi,[2] Pavel B. Ryzhakov,[1,2,a)] and Jordi Pons-Prats[2,3]

AFFILIATIONS

[1]Universitat Politècnica de Catalunya - BarcelonaTech (UPC), Escola Tècnica Superior d'Enginyers de Camins, Canals i Ports, C/Jordi Girona 1, Campus Nord UPC, 08034 Barcelona, Spain
[2]Centre Internacional de Mètodes Numérics en Enginyeria (CIMNE), C/Gran Capitán s/n, Campus Nord UPC, 08034 Barcelona, Spain
[3]Department of Physics, Aeronautics Division, Universitat Politècnica de Catalunya, Barcelona Tech (UPC), Edifici C3, Esteve Terrades, 5, 08860 Castelldefels, Spain

[a)]**Authors to whom correspondence should be addressed:** cnarvaez@cimne.upc.edu and pavel.ryzhakov@upc.edu

ABSTRACT

In this work, a numerical model for the simulation of two-phase electrohydrodynamic (EHD) problems is proposed. It is characterized by a physically consistent treatment of surface tension as well as a jump in the electric material properties. The formulation is based on a finite element method enriched with special shape functions, capable of accurate capturing discontinuities both in the fluid pressure and the gradient of the electric potential. Phase interface is, thus, represented as a zero-thickness boundary. The proposed methodology allows modeling the electric force as an interfacial one, strictly abiding with the physics. The approach is tested using the droplet deformation benchmarks. Moreover, application of the method to study a three-dimensional (3D) case, not characterized by symmetry of revolution, is shown. The proposed methodology defines a basis for an enriched finite element method for a wide range of EHD problems.

I. INTRODUCTION

During the last decade, electrohydrodynamics (EHD) in multiphase microsystems has become a topic of active research.[1–4] The numerical modeling of such systems is becoming of particular importance for modern manufacturing techniques.[5–7] In EHD studies, one is typically interested in the analysis of droplet dynamics under the effect of an electric field. Despite the progress made in the field, one of the main complexities that typically undermines the quality of the numerical simulations of EHD problems is the presence of strong and/or weak discontinuities in the fluid and electrical fields. These discontinuities cannot be adequately represented by the majority of the existing classes of numerical methods (finite elements, finite volumes, and finite differences) *per se* and require introducing special additional techniques.

Several classes of numerical schemes have been reported in the literature for treating such discontinuities. Based on how the interface is treated, the most common classes of methods are level-set,[8–12] volume-of-fluid,[13–15] and phase-field.[16,17] Other methods include the lattice-Boltzmann,[18,19] smoothed-particle-hydrodynamics,[20,21] Immerse Interface Method (IIM),[9,22] embedded Eulerian–Lagrangian,[23,24] and Particle Finite Element Method (PFEM),[25,26] to name just a few. In addition to the most common techniques listed above, some other methods applied to the problem of interest include the Boundary Element Method (BEM);[27,28] however, application of this latter methodology is restricted to problems with minor topological changes.

One of the critical issues related to the choice of the particular scheme among the above-mentioned ones is the handling of the electric force, which corresponds to the discontinuity in Maxwell stress tensor. The electric force can be computed either as an interfacial force ("jump" in the Maxwell stress tensor across the interface $[\![\mathbf{n}\cdot\mathbb{T}_e]\!]$) or as a volume (body) force expressed as divergence, $\nabla\cdot\mathbb{T}_e$, of Maxwell tensor.[29,30] Most of the numerical studies cast the electric effect as a volume force, smearing it over a region of finite thickness due to its simplified computational treatment. However, in light of the early studies of EHD, it was shown that the electro-hydrodynamic interactions at the interface dominate the resulting two-phase system.[31,32] Consequently, computing the electric force on the basis of Maxwell tensor smoothed over a few cells/elements obliges using very fine meshes at the interface, otherwise, a large error is introduced in the interface proximity.[22] Due to electro-mechanical coupling, this, in turn, leads to inaccurate solution of the momentum equation.

The errors become particularly severe if the difference in the electric properties of the fluids involved is large.

In the present work, we strive to develop an efficient and robust alternative to the existing approaches. Our model is based on the Finite Element Method (FEM) equipped with the level-set approach[33] for capturing the sharp material interface. The discontinuity in the material properties (both mechanical and electric) is represented in the Enriched Finite Element Method (EFEM) fashion,[34–36] via introducing and then condensing additional degrees of freedom in the elements cut by the interface between the fluids. The electro-hydrodynamic coupling is implemented by incorporating the electric force in the momentum equation of the fluid as a surface (and not volumetric) integral ensuring the accurate representation of the corresponding term even on coarse meshes.

The paper begins with the governing equations (Sec. II). The enrichment of the finite element spaces is presented. Particular attention is paid to the electro-mechanical coupling. In Sec. III, the method is validated and tested using several numerical examples. Its application to analysis of droplets deforming under the effect of electric field is shown in two and three dimensions. Finally, summary and conclusions are given in Sec. IV.

II. NUMERICAL METHOD

A. Problem statement

Let us consider two immiscible fluids (Ω_1 and Ω_2) separated by an interface (Γ) and exposed to electric field ($\mathbf{E}$) as shown in Fig. 1. Due to the action of the electric field, the fluid molecules may get polarized and the charged ions/free electrons migrate to the interface, thereby the fluids are set in motion.[31,32] In order to model such phenomenon, the system must be described by the conservation equations governing the fluid flow on the one hand and the electric field on the other hand.

The mass and momentum conservation equations for the fluid flow read

$$\nabla \cdot \mathbf{u} = 0 \tag{1}$$

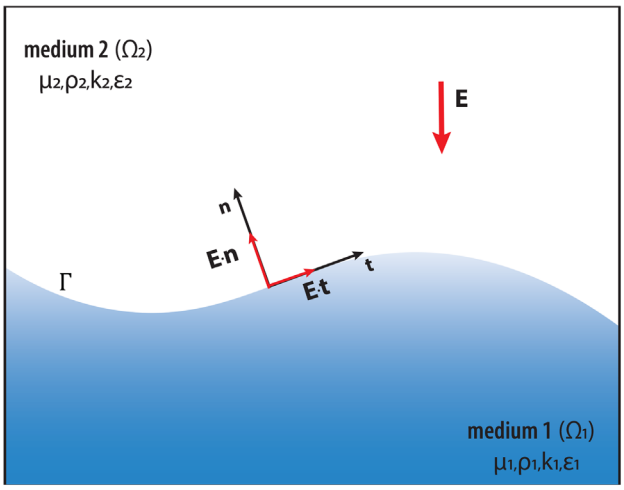

FIG. 1. A scheme of a two-phase domain exposed to electric field.

and

$$\frac{\partial \rho \mathbf{u}}{\partial t} + \rho \mathbf{u} \cdot \nabla \mathbf{u} = \nabla \cdot \boldsymbol{\sigma} + \mathbf{f}, \tag{2}$$

respectively. Here, ρ is the density, $\mathbf{u}$ is the velocity vector, $\mathbf{f}$ is a vector of external body forces, and $\boldsymbol{\sigma}$ is the total stress tensor. In the case of Newtonian fluids, the total stress tensor is

$$\boldsymbol{\sigma} = -p\mathbb{I} + \mu(\nabla \mathbf{u} + \nabla \mathbf{u}^T), \tag{3}$$

where p is the pressure, μ is the dynamic viscosity, and $\mathbb{I}$ is the identity tensor. Physical properties are determined according to the subdomains, e.g., $\rho = \rho_1$ in Ω_1 and $\rho = \rho_2$ in Ω_2.

The electromagnetism is described by Maxwell's equations. Nonetheless, for modeling the EHD flow, the magnetic effects are commonly neglected and the electrostatic equations provide sufficiently accurate results taking into account that the characteristic timescale for the magnetic field is significantly smaller than that of the electric field.[37] It should also be noted that common EHD applications are basically studied in the absence of external magnetic fields. Omitting the magnetic field, Maxwell–Faraday equation for electric field $\mathbf{E}$ becomes

$$\nabla \times \mathbf{E} = 0, \tag{4}$$

and, therefore, electric potential ϕ can be introduced as

$$\mathbf{E} = -\nabla \phi. \tag{5}$$

For leaky dielectric model,[14,31,37] that is known to realistically represent the behavior of liquids in common EHD applications, the conservation of the electric current reads[38]

$$\nabla \cdot \mathbf{J} = 0, \tag{6}$$

where $\mathbf{J} = \kappa \mathbf{E}$, with κ being the electric conductivity. Note that the convection of the bulk free charge density is neglected for the small value of the so-called "electric Reynolds number."[38]

Substituting Eq. (5) into Eq. (6), one obtains

$$\nabla \cdot (\kappa \nabla \phi) = 0. \tag{7}$$

In this work, Eq. (7) is subject to Dirichlet boundary condition as follows:

$$\phi = \tilde{\phi} \quad \text{on } \partial\Omega_{elec,D}. \tag{8}$$

For the sake of simplicity, trivial Neumann condition ($\mathbf{n} \cdot \nabla \phi = 0$) is considered for the rest of the domain boundary ($\partial\Omega \backslash \partial\Omega_{elec,D}$).

Moreover, the continuity of the electric potential and the electric current is required at the interface ($\Gamma = \Omega_1 \cap \Omega_2$)[31]

$$[\![\phi]\!] = 0, \tag{9}$$

$$\mathbf{n} \cdot [\![\mathbf{J}]\!] = 0, \tag{10}$$

where $\mathbf{n}$ is the normal unit vector to Γ and $[\![\cdot]\!]$ is the "jump" operator.

B. Electro-hydrodynamic coupling

In EHD applications, the electric field and the hydrodynamics are coupled via the electric force, which can be calculated using the well-known electric Korteweg–Helmholz force.[31] For an incompressible electrically linear material, this coupling force is

$$\mathbf{f}_e = \rho_e \mathbf{E} - \frac{1}{2}(\mathbf{E}\cdot\mathbf{E})\nabla\epsilon, \tag{11}$$

with ρ_e being the electric charge density. Neglecting the convection of the charge density, $\mathbf{f}_e$ becomes zero everywhere in the domain except the interface, which is characterized by a jump in the electric permittivity (ϵ).

Equation (11) can equivalently be written as $\mathbf{f}_e = \nabla\cdot\mathbb{T}_e$ with the Maxwell stress tensor defined as

$$\mathbb{T}_e = \epsilon\mathbf{E}\otimes\mathbf{E} - \frac{1}{2}\epsilon(\mathbf{E}\cdot\mathbf{E})\mathbb{I}. \tag{12}$$

Using this definition, the electric force can be directly calculated as interfacial force per area[14,37]

$$\tilde{\mathbf{f}}_e = \mathbf{n}\cdot[\![\mathbb{T}_e]\!]. \tag{13}$$

C. Finite element formulation

The weak form of the governing equations [Eq. (7) (conservation of electric current), Eq. (1) (mass conservation), and Eq. (2) (momentum conservation)] can be written, respectively, as

$$\int_\Omega \nabla s\cdot(\kappa\nabla\phi)d\Omega = 0, \tag{14}$$

$$\int_\Omega q\rho(\nabla\cdot\mathbf{u})d\Omega = 0, \tag{15}$$

$$\begin{aligned}\int_\Omega \rho\left(\frac{\partial\mathbf{u}}{\partial t}+\mathbf{u}\cdot\nabla\mathbf{u}\right)\cdot\mathbf{w}d\Omega = &-\int_\Omega p\nabla\cdot\mathbf{w}d\Omega \\ &+\int_\Omega \mu(\nabla\mathbf{u}+\nabla\mathbf{u}^T):\nabla\mathbf{w}d\Omega \\ &+\int_\Gamma \mathbf{w}\cdot\mathbf{t}d\Gamma,\end{aligned} \tag{16}$$

where s, q, and w are the test functions.

The last term on the right-hand-side of Eq. (16) accounts for Neumann condition, representing the net traction at the interface between the two material domains

$$\mathbf{t}(\mathbf{x},t) = \tilde{\mathbf{f}}_e - \gamma K(\mathbf{x})\mathbf{n}, \tag{17}$$

where γ is the surface tension coefficient and K is the curvature. Definition of an accurate Finite Element model on the basis of Eqs. (14)–(16) on a fixed mesh requires special treatment of discontinuities in the gradient of the electric potential (ϕ) and the pressure (p) at the material interface. The former occurs due to the jump in the electric material properties (conductivity/permittivity), while the latter one is the result of the presence of surface tension. In order to tackle this challenge, in the present work, the finite element spaces used for the approximation of ϕ and p are enriched by shape functions that are specifically developed for representing mentioned discontinuities.[36,39] The proposed enriched approximations in cut elements (i.e., elements, crossed by the interface, Γ) are

$$\phi^h(x) = \underbrace{\sum_{i\in e.n} N_i(x)\phi_i}_{standard} + \underbrace{\bar{N}_\phi(x)\phi^*}_{enriched}, \tag{18}$$

$$p^h(\mathbf{x},t) = \underbrace{\sum_{i\in e.n} N_i(\mathbf{x})p_i(t)}_{standard} + \underbrace{\sum_{i\in e.n} \bar{N}_{p,i}(\mathbf{x})p_i^*(t)}_{enriched}, \tag{19}$$

where N_i is the standard finite element shape function, and ϕ_i and p_i are the values corresponding to node i of the element. The enrichment terms are defined by the enrichment shape functions $\bar{N}_\phi(x)$, $\bar{N}_{p,i}(x)$ and the additional degrees of freedom, ϕ_i^* and p_i^*. The corresponding enrichment functions for the electric potential and pressure are presented in Eqs. (20) and (21), respectively. Note that the electric potential space is enriched with only one additional degree of freedom, while the pressure field with three additional degrees following Refs. 36 and 39, respectively. The enriched shape functions are defines as

$$\bar{N}_\phi(x) = \sum_{i\in e.n} N_i(x)|\psi_i(x)| - \left|\sum_{i\in e.n} N_i(x)\psi_i(x)\right| \tag{20}$$

and

$$\bar{N}_{p,i}(x) = \frac{1}{2}H(\mathbf{x})(H(\mathbf{x}) - H(\mathbf{x}_i))N_i(\mathbf{x}), \tag{21}$$

with

$$H(\mathbf{x}) = \begin{cases} 1 & \text{if} \quad \psi(\mathbf{x}) > 0 \\ -1 & \text{if} \quad \psi(\mathbf{x}) \le 0 \end{cases}, \tag{22}$$

where $\psi(x)$ is the signed distance function. The evolution of ψ is captured via the level-set method[33] following the standard scheme based on the advection equation as

$$\frac{\delta\psi}{\delta t} + \mathbf{u}\cdot\nabla\psi = 0. \tag{23}$$

The schematic representation of the enrichment functions is illustrated in Fig. 2. Figure 2(a) illustrates the finite element mesh and the position of the phase interface. Figure 2(b) shows the enrichment shape functions for capturing the weak discontinuity in the electric potential across the interface in the cut element. Figure 2(c) illustrates the enrichment of strong pressure discontinuity.

D. Solution algorithm

To this end, the main ingredients of the model are specified. In the following, the overall solution algorithm is presented. Note that the system of equations solved at each solution step is obtained based on the standard finite element scheme using the weak forms of the governing equations and the finite element spaces presented above. The details of the time discretization as well as the stabilization of the momentum equation can be consulted in Ref. 39.

The solution of the EHD problem following the present model is shown in Table I. Note that after adding the enrichment contributions in the cut elements, these are statically condensed prior to assembly as shown in Ref. 39 (for the fluid problem) and Ref. 40 (for the electric potential).

III. NUMERICAL EXAMPLES

In this section, we first present examples for assessing the proposed enriched finite element method/level-set approach, estimating the error in the electric field and interfacial electric force. Afterward, we simulate droplets exposed to electric field in both two- and three-dimensional. The model was implemented by the authors in Kratos Multiphysics, an in-house Open Source C++ object-oriented Finite Element framework.[41,42]

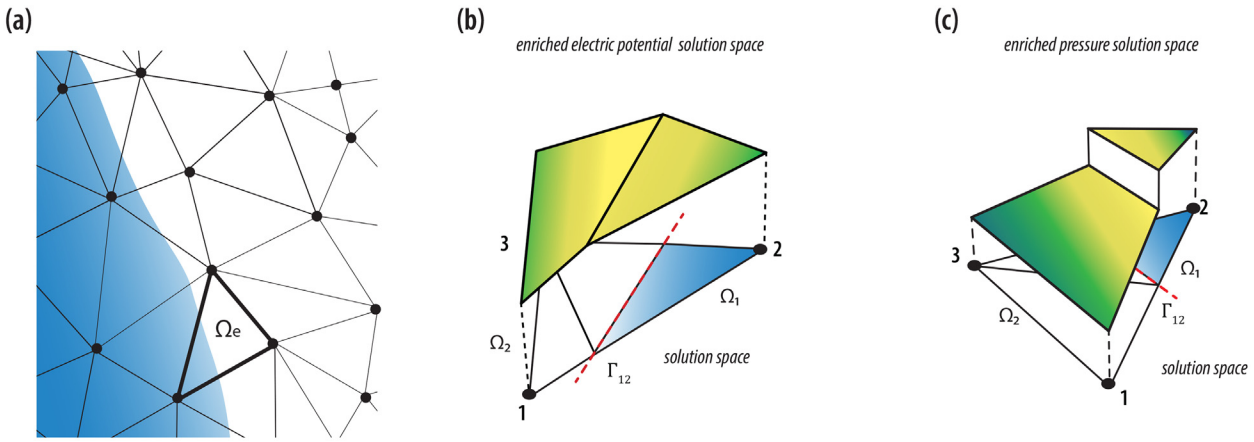

FIG. 2. Schematic representation of the solution space enrichment. (a) FE mesh and interface position. (b) Enrichment shape function for electric potential. (c) Enrichment shape function for the pressure field.

A. Domain with a horizontal interface in an electric field

The first test validates the electric equations in one dimension. It is performed following the configuration proposed in Refs. 13 and 14. Here, the domain contains two different homogeneous and immiscible media separated by a horizontal interface located at the mid-height of the domain as shown in Fig. 3. Electric potentials of 1 and 0 V are applied to the two parallel electrodes coinciding with the bottom and top walls of a unit square, resulting in an electric force that can be described by the conductivity ratio $R = \kappa_1/\kappa_2$ and permittivity ratio $Q = \epsilon_1/\epsilon_2$. The indices 1 and 2 correspond to the lower and upper sub-domain, respectively. For the numerical test, the parameters have been set to the values presented in Table II.

The comparison between the results obtained using the proposed EFEM and the exact solution (see Table II) is shown in Fig. 4. As can be seen from the analytic solution the electric potential decreases linearly along Y direction, however, the slope changes precisely at the cut (Y = 0.5 m). This kink in the electric potential brings in a jump in its gradient (**E**). Note that the additional degree of freedom (ϕ^*) is adjoined to the results of the EFEM. It was "recovered" after solving the system so that the value can be evaluated exactly at the cut (where no actual node is located). The benefit of the additional degree of freedom becomes evident when looking at the electric field distribution [dashed lines in Fig. 4(b)]. One can see that the "jump" is reproduced exactly.

For the purpose of analysis, the interfacial electric force ($\mathbf{n} \cdot [\![\mathbb{T}_e]\!]$) was calculated and compared with the exact value that is inferred from the traction vector as follows:

$$[\mathbf{n} \cdot \mathbb{T}_e]^{ex} = \frac{1}{2}\left[\epsilon_2(\mathbf{E}_2 \cdot \mathbf{n})^2 - \epsilon_1(\mathbf{E}_1 \cdot \mathbf{n})^2\right]. \tag{24}$$

The numerical results for both the electric potential distribution [Fig. 4(a)] and the gradient of electric potential [Fig. 4(b)] stand out

TABLE I. Summary of the proposed method.

Algorithm 1: Summary of the proposed EFEM for EHD problems

while *time* < *run-time* **do**
- **solve** Level Set Eq. (23) to find new position of the phase interface ψ;
- **compute** elemental Laplace Eq. (14);
  - **for** *cut elements* **do**
    - **add** enrichment contributions for electric potential ϕ (following Eq. (20));
- **assemble and solve** Laplace Eq. (14) for ϕ;
- **compute** electric field **E** following Eq. (5);
- **compute** elemental mass/momentum conservation system [Eqs. (15) and (16)];
  - **for** *cut elements* **do**
    - **add** enrichment contributions for the pressure p [following Eq. (19)];
    - **add** the electric force and surface tension contributions Eq. (17) to momentum Eq. (16);
- **assemble and solve** mass/momentum system [Eqs. (15) and (16)] for velocity **u** and pressure p;

go to next time step

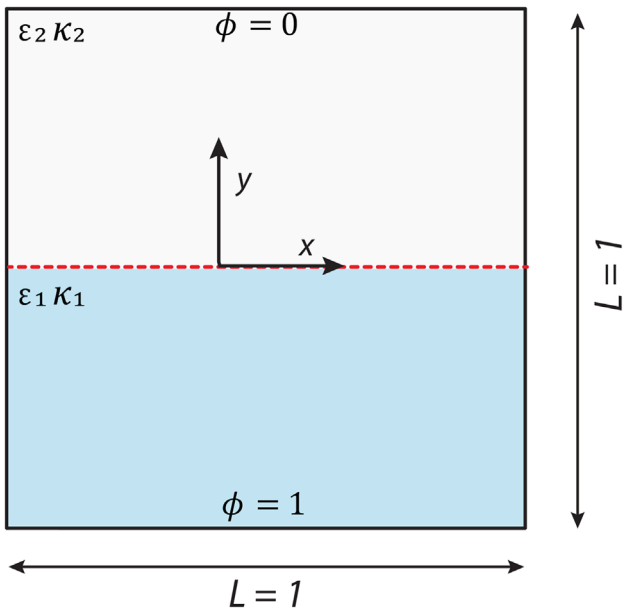

FIG. 3. Planar problem: two materials with different electric properties.

TABLE II. Analytic dimensionless solution for the bi-material planar cases following Ref. 14.

Property	ϕ_1^{ex}	ϕ_2^{ex}	E_1^{ex}	E_2^{ex}	$[\mathbf{n}\cdot\mathbb{T}_e]$
$R=1e^6$, $Q=3$	1	$-2y+1$	0	2	2

because they do not exhibit deviations from the exact solution, even though they were obtained on a very coarse grid. The errors in the computed electric field are shown in Table III).

B. Electric force around a droplet

In the following example, we analyze the interfacial electric force distribution using the settings shown in Fig. 5. A droplet of radius

TABLE III. Deviations from the exact solution of **E** and $[\mathbf{n}\cdot\mathbb{T}_e]$ at the cut elements. Note: that the zero means that the simulation meet up the floating-point accuracy of the computer.

	Error (%) $\lvert 1-E/E^{ex}\rvert$		Error (%) $\lvert 1-[\mathbf{n}\cdot\mathbb{T}_e]/[\mathbf{n}\cdot\mathbb{T}_e]^{ex}\rvert$
Grid size	E_1	E_2	
3×3 ($h\approx0.3$)	⋯	0	0
5×5 ($h\approx0.2$	⋯	0	0
33×33 ($h\approx0.03$)	⋯	0	0

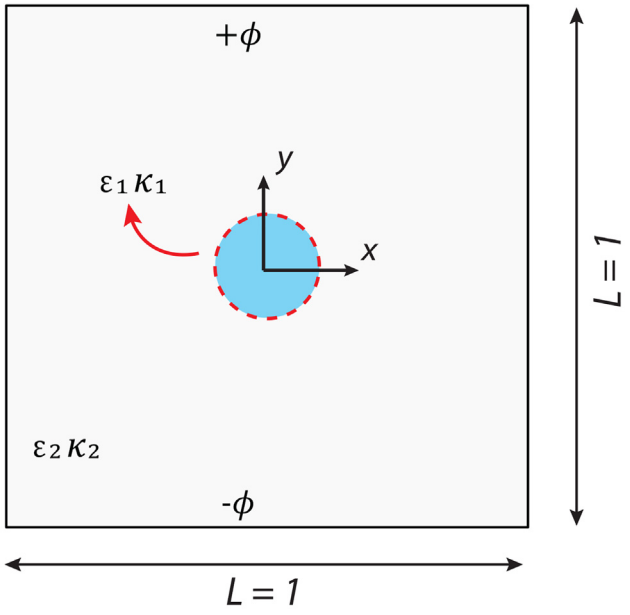

FIG. 5. Square domain with a circular droplet.

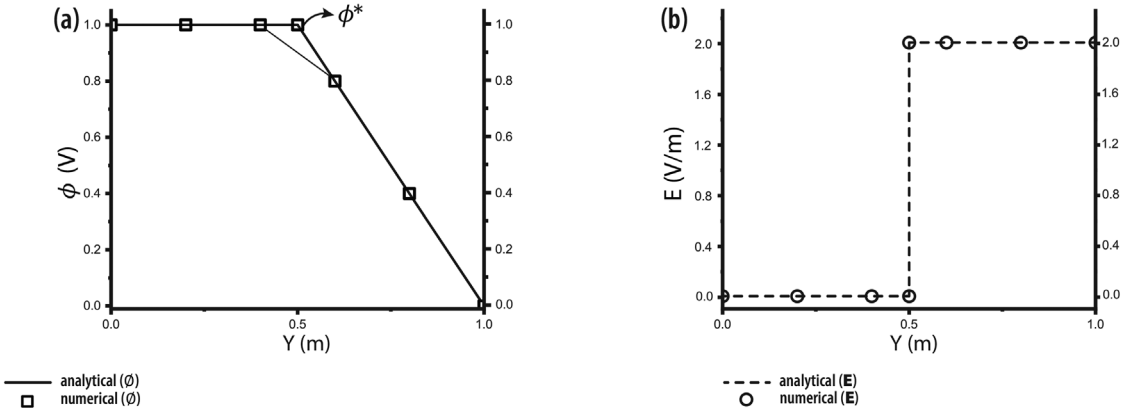

FIG. 4. Numerical results of the planar problem along the vertical cut ($Y=0.5$). (a) Distribution of the electric potential (ϕ). (b) Electric field (**E**).

TABLE IV. Electric properties of the media used.

System	$Q = \epsilon_1/\epsilon_2$	$R = \kappa_1/\kappa_2$	Reference
S1 ($Q = R$)	0.5	0.5	...
S2 ($Q > R$)	0.821	0.252	43
S3 ($Q < R$)	1.218	3.970	43

$R_o = 0.1(m)$ is located at the middle of a unit square domain. In all simulations, the electric potentials of 1 and 0 V are applied to the top ($+\phi$) and bottom ($-\phi$) walls, respectively. The solution was assayed for three case-studies: $Q = R$ (S1), $Q > R$ (S2), and $Q < S$ (S3). Table IV provides the physical properties of each medium for all the cases studied. The contours of the electric potential for the three systems are presented in the first row of Figs. 6(a)–6(c). One can see, for S1 and S2, the contours of electric potential are relatively straight equispaced horizontal lines, which suggest that the electric potential varies almost linearly in the direction of the field. For S3, the contour lines are lest concentrated in the cylinder and they tend to conform the cylinder shape,

$$\mathbf{T}_e^{ex} = \frac{2\epsilon_2 \mathbf{E}_\infty^2}{(R+1)^2}\left(\left[Q-1+(R^2+1-2Q)\cos^2\theta\right]\mathbf{n} + \left[(Q-R)\sin 2\theta\right]\mathbf{t}\right). \tag{25}$$

The distribution of the interfacial electric force is shown in the second row of Figs. 6(d)–6(f). For the system *S1*, where the ratios of permittivity and conductivity are equal ($Q = R$), the tangential component of the electric force is zero. Therefore, the electric force is perpendicular to the droplet interface. Being Q and R equal, the sign of the force depends on the value of Q. The normal electric force is directed

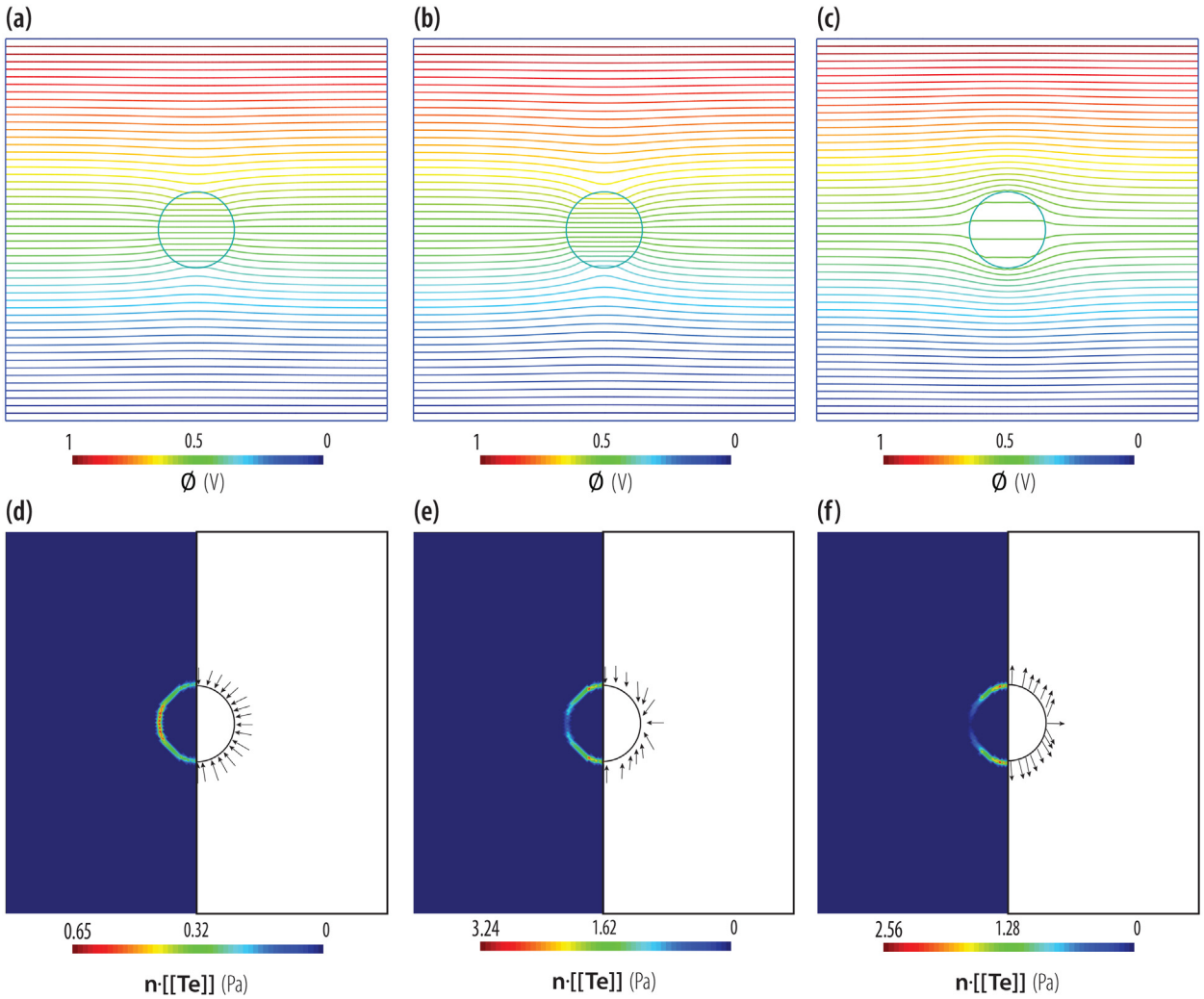

FIG. 6. Different droplet systems (S1, S2, and S3) under an electric field ($\mathbf{E}_\infty = 1$). (a) and (b) electric potential for systems S1, S2, and S3, respectively. (d)–(f) Corresponding distribution of the electric force at the interface.

from the media of higher permittivity toward the one with lower permittivity [see Fig. 6(d)]. On the other hand, in systems *S2* and *S3*, a non-zero tangential component can appear. Depending on the relative magnitude of Q and R, the droplet undergoes tension or compression [see Figs. 6(e)–6(f)]. This observation confirms that both R and Q affect the droplet deformation mode.

A further comparison between the exact solution [Eq. (25)] and the numerical one obtained on a mesh with element size (h= 0.075, 0.018 75, and 0.009 375) was performed. The measured error at the pole ($\theta = 0$) is provided in Table V. One can see that with mesh refinement the accuracy increases, reaching the value of $\leq$2% for the finest mesh used. Note that smeared interface approach requires substantially finer meshes in the vicinity of the interface in order to reach results with similar accuracy.[44]

C. Deformation of a droplet subjected to an electric field

In this example, the impact of electric field on the droplet dynamics is analyzed using a square domain $\Omega = (0,1) \times (0,1)$ equivalent to the one shown in Fig. 5. The circular subdomain represents the droplet with the radius $R_o = 0.1(m)$, suspended in a continuous phase (outer fluid). Both phases are separated by an interface (discontinuous line) with surface tension coefficient γ. The droplet and the continuum phase are assumed to be immiscible with homogeneous physical properties (ϵ, κ, ρ, and μ). Based on these properties, the following parameters can be defined: $Q = \epsilon_1/\epsilon_2$, $R = \kappa_1/\kappa_2$ and $\beta = \mu_1/\mu_2$, where β is the viscosity ratio. An additional dimensionless parameter is the electric capillary number ($Ca_E = \mathbf{E}_\infty^2 R_o \epsilon_2/\gamma$), which compares the electric stress and the capillary force. The used values of the aforementioned parameters will be defined below.

Once the electric potential is applied to the parallel electrodes $+\phi$ and $-\phi$, the droplet begins to deform reaching eventually either oblate- or prolate-type shape, or may remain spherical. However, if the value of the electric potential is large enough, the droplet no longer reaches a steady configuration. In such case large deformations and/or droplet breakup are expected. The literature devoted to the droplet systems usually quantifies the droplet deformation by $D = (b-a)/(b+a)$, where b and a are the droplet lengths parallel and perpendicular to the electric field, respectively. Note that prolate-type deformation corresponds to the positive value ($D > 0$), while a negative ($D < 0$) value corresponds to an oblate-type deformation.

In order to validate the model, the deformation of a castor oil droplet embedded in silicone oil was simulated reproducing the experimental study reported in Ref. 45. The parameters are given in Table VI (corresponding to NN21 case in Ref. 45). According to the reported experimental data, the droplet with initial radius of 1.6 mm is located at the middle of the domain spanned between two parallel electrodes. Upon the imposition of the electric field, the droplet becomes elongated and reaches a terminal elliptical shape for constant electric field.

TABLE V. Deviation from the exact solution of the electric force at the interface along $\theta = 0$ transect.

S1		S2		S3	
R_o/h	$\lvert 1 - [\mathbf{n}\cdot\mathbb{T}_e]/\mathbf{T}_e^{ex}\rvert$	R_o/h	$\lvert 1 - [\mathbf{n}\cdot\mathbb{T}_e]/\mathbf{T}_e^{ex}\rvert$	R_o/h	$\lvert 1 - [\mathbf{n}\cdot\mathbb{T}_e]/\mathbf{T}_e^{ex}\rvert$
≈ 1.5	0.221	≈ 1.5	0.361	≈ 1.5	0.193
≈ 5.5	0.107	≈ 5.5	0.131	≈ 5.5	0.109
≈ 11	0.02	≈ 11	0.006	≈ 11	0.003

TABLE VI. Physical properties of the system extracted from Ha and Yang's experimental study.[45]

System	Q	R	β	γ (N/m)
NN21	$\approx$10	1.37	0.874	3.3×10^{-3}

Figure 7 shows the variation of the deformation parameter as a function of the electric capillary number. For the largest value of $Ca_E = 0.13$, the error is approximately 6%. Overall, the obtained results show good agreement with the experimental data.

What follows is a further validation of the proposed method, here, the deformation parameter D obtained in the numerical simulation is compared with the theoretical value, obtained by applying an expression developed for small droplet deformations according to the following equation:[46]

$$D_{Feng} = \frac{R^2 + R + 1 - 3Q}{3(1+R)^2} Ca_E. \tag{26}$$

The numerical solution is obtained for the values of dimensionless parameters proposed in Ref. 47 (which correspond to an oblate-type deformation): $Ca_E = 0.1$, $Q = 3.5$, $R = 1.75$, $\beta = 1$, and $\gamma = 0.1$. The same case is simulated using two meshes: a coarser ($R_o/h \approx 8$) and finer ($R_o/h \approx 16$) one. The resulting deformations are $D = -0.0193$ and $D = -0.0202$ for $R_o/h = 8$ and $R_o/h = 16$, respectively. One can see in Table VII that similar results were reported in the literature. Comparing our results with the reference solution $D_{Feng} \approx -0.0207$, one can see that numerical result agrees

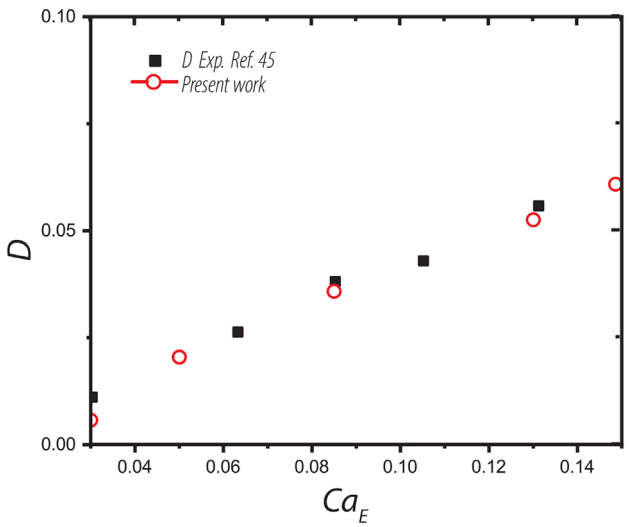

FIG. 7. Deformation as function of Ca_E of NN21 system.

TABLE VII. Quantitative comparison of the deformation factor from the present work with the analytical solution and previous numerical results.

			Deformation factor D					
Q	R	Ca_E	Analytical[46]	Ref. 47	Ref. 48	Ref. 49	Present ($R_o/h = 8$)	Present ($R_o/h = 16$)
3.5	1.75	0.1	−0.0207	−0.0200	-0.0220	−0.0223	−0.0193	−0.0202

well with the theoretical prediction. Since the results obtained with $R_o/h = 8$ are acceptable (≈ 6% error), this mesh resolution will be used henceforth due to the lower computational cost associated.

Next test case simulated corresponds the prolate-type deformation with the following parameters: $Ca_E = 0.1$, $Q = 2$, $R = 2.5$, and $\beta = 1$. For this case, the numerical solution on the coarse mesh ($R_o/h \approx 8$) is $D = 0.0118$, while the reference deformation is $D_{Feng} \approx 0.0102$. Again, the obtained deformation acceptably agrees with the reference one. It is worth noting that comparable accuracy could be achieved using existing approaches reported in the literature for much finer meshes, $R_o/h \geq 20$[50,51] or even finer.[52]

Further simulations were conducted for prolate- and oblate-type deformations by increasing Ca_E. Figure 8(a) shows the summary of the results and the comparison with the analytical expressions proposed by Feng,[46] Taylor,[53] and Ajavi.[54] The latter model includes the second-order terms and further improves the accuracy of Taylor's model for the finite droplet deformation. In Fig. 8(a), the results of the proposed method are compared with the above-mentioned analytical models as well as several numerical approaches reported in the literature.[47–49] Both prolate and oblate cases are included.

It is seen that the results of the proposed method agree well with the three theoretical expressions up to $Ca_E = 0.1$. However, by increasing the electric capillary number, the discrepancy between the predictions of the linear theories (Feng[46] and Taylor[53]) and the numerical solutions becomes more significant. This is particularly evident for $Ca_E > 0.3$. Beyond $Ca_E = 0.7$, the results further deviate from those of the second-order variant of the Taylor's theory.[54] A similar trend is seen in Fig. 8(a) for the results of other numerical approaches included in this figure. It is worth to mention that the analytical models were developed under the assumption of small deformation that is not fulfilled for large Ca_E.[9,52,55] The initial and equilibrium configurations of the droplet are shown in Fig. 8(b) for three values of Ca_E. The results in the present work have been obtained in the present work for up to $Ca_E = 2$, while for the other numerical methods, reported in the references the maximum electric capillary number considered was $Ca_E = 1$. Therefore, the result corresponding to $Ca_E = 2$ is shown only in Fig. 8(b).

Figure 9 illustrates the velocity vectors (left half) and velocity field contour (right half) for three different values of Ca_E (0.5, 1, and 2). The velocity vector (left) and colored contours of velocity magnitude (right) are plotted under steady state deformation for $Ca_E = 0.5$ (first column), $Ca_E = 1$ (second column), and $Ca_E = 2$ (third column).

The first and the second rows correspond to the prolate- and oblate-type deformation, respectively. The convective flow that occurs due to a re-circulation inside and outside the droplet is from the pole to the equator when $R < Q$ (prolate-type). On the contrary, when $R > Q$ (oblate-type) a reversed flow is generated. In addition, note that the convective flow becomes stronger with increasing Ca_E. These results agree with previous findings.[47,50–52,55]

D. 3D simulations of a droplet subjected to an electric field

Next, we simulate the droplet deformation in 3D. In this example, the computational domain is $\Omega = (0, 1) \times (0, 1) \times (0, 1)$ where the droplet with radius $R_o = 0.1$ is centered at $(0.5, 0.5, 0, 5)$. The test is solved varying the ratio of the conductivity of the two fluids (droplet and the surrounding). The external electric field is imposed by setting the electric potential to $+\phi$ and $-\phi$ at top and bottom faces, respectively. Figure 10 shows the initial configuration of the 3D domain. Two settings are considered: in the first one, droplet is located exactly

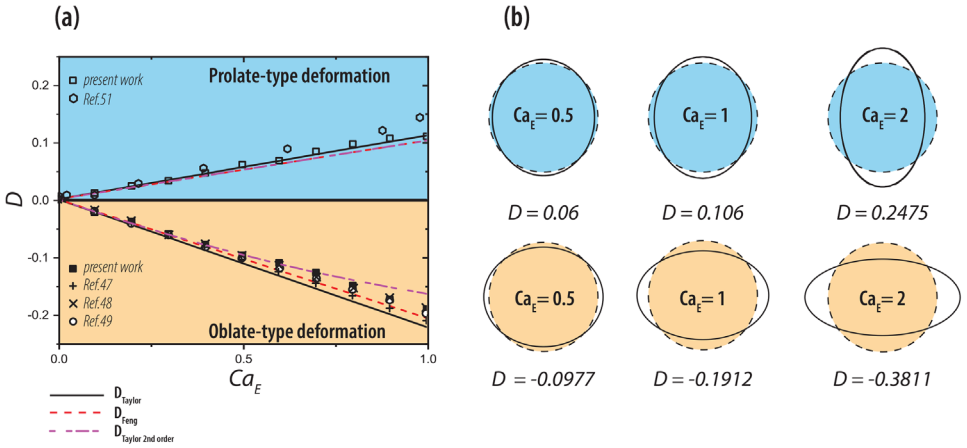

FIG. 8. Deformation as function of Ca_E for oblate-type ($Q = 3.5$ and $R = 1.75$) and prolate-type ($Q = 2$ and $R = 2.5$). (a) Solid and dashed lines are the theoretical predictions. (b) Initial (dashed line) and equilibrium (continuous line) droplet shapes.

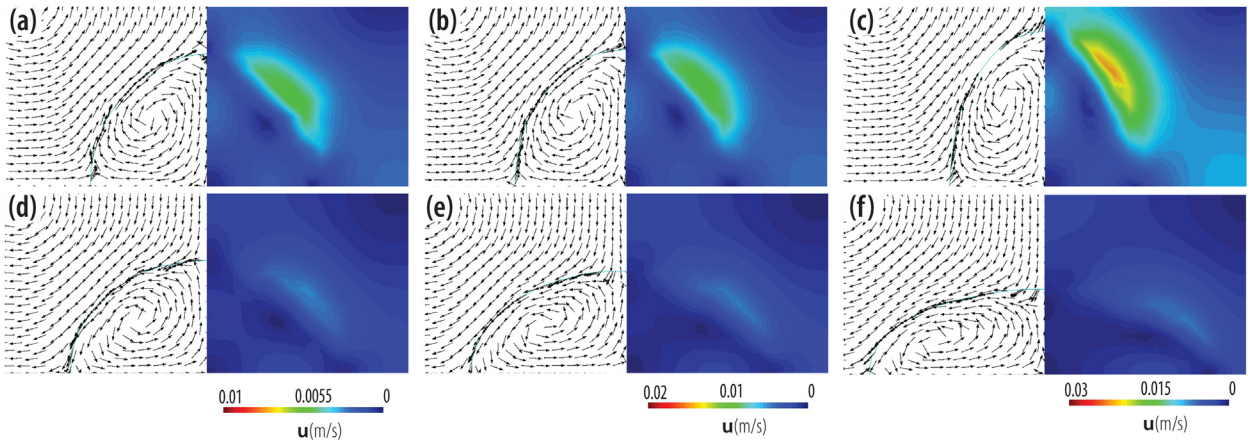

FIG. 9. Induced convective flow pattern in prolate-type [first row (a)–(c)] and oblate-type [second row (d)–(f)].

at the center of the domain, and in the second one the droplet is moved toward one of the vertical walls (parallel to the XY plane).

The parameters of the test are set as $Ca_E = 1$, $Q = 3.5$, and $\beta = 1$ in order to ensure large deformation of the droplet. In case the conductivity of the droplet dominates that of the surrounding, the accumulation of charges at the liquid-gas interface leads to attractive forces predominantly in the direction toward the electrodes. Consequently, the droplet stretches and for rather large conductivity ratios, e.g., $R = 10$ as used here, a stick-like shape is formed as shown in Fig. 11. In the opposite situation, i.e., for dominant gas conductivity, repulsive forces pushes the droplet toward the center along with the imposed external electric field. Thus, a compressed wheel-like shape is formed for $R = 0.1$ (see Fig. 12). Similar observations were reported in the literature.[56]

In general, modeling either disk-type or the elongated deformation by approaches that couple the electric body force is challenging, because its solution requires higher grid refinements in order to capture the sharp variations of physical quantities. The present results are significant since they demonstrate the ability of the present approach of resolving these challenging cases without incurring into necessity of using excessively refined meshes.

In order to show the capability of the proposed method in a more complex configuration, a 3D test case is solved placing the droplet being close to one of the walls, centered at $(0.5, 0.5, 0, 175)$ [see Fig. 10(b)]. The parameters used are $Ca_E = 1$, $Q = 3.5$, $R = 10$, and $\beta = 1$. The droplet is intentionally displaced away from the center in order to induce an asymmetry in the problem. For the present case, the direction of the electric force is similar to the previous example, which is toward the poles [see Fig. 13(a)]. As was expected, the presence of the wall disturbs the symmetry of the electric field and consequently leads to an unevenly distributed electric force as observed in Figs. 13(e)–13(i). This deviation from the symmetry creates an eccentricity along the longitudinal line as shown in Fig. 13(i)–13(l).

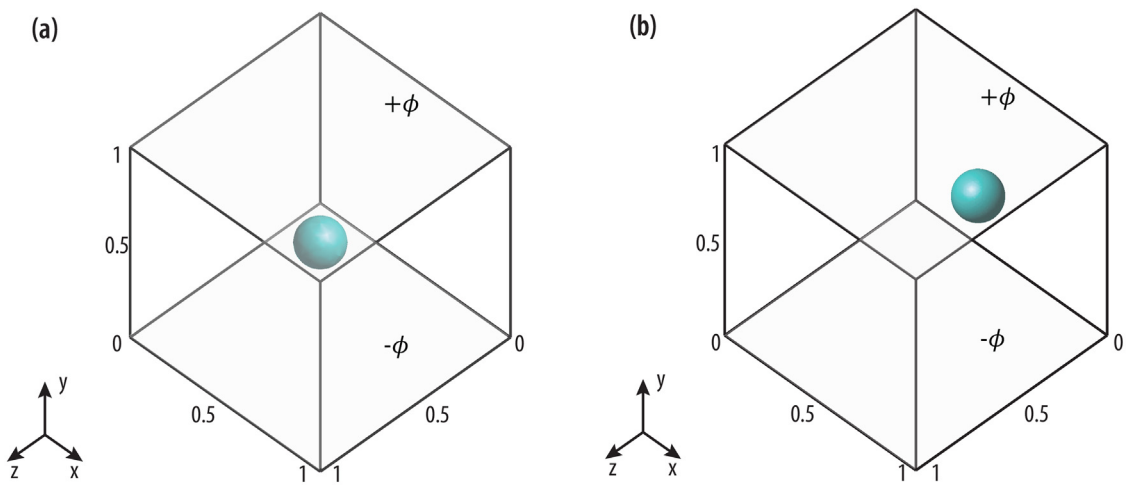

FIG. 10. Sketch of the 3D problem. (a) Droplet placed at the center and (b) droplet placed in the vicinity of a wall.

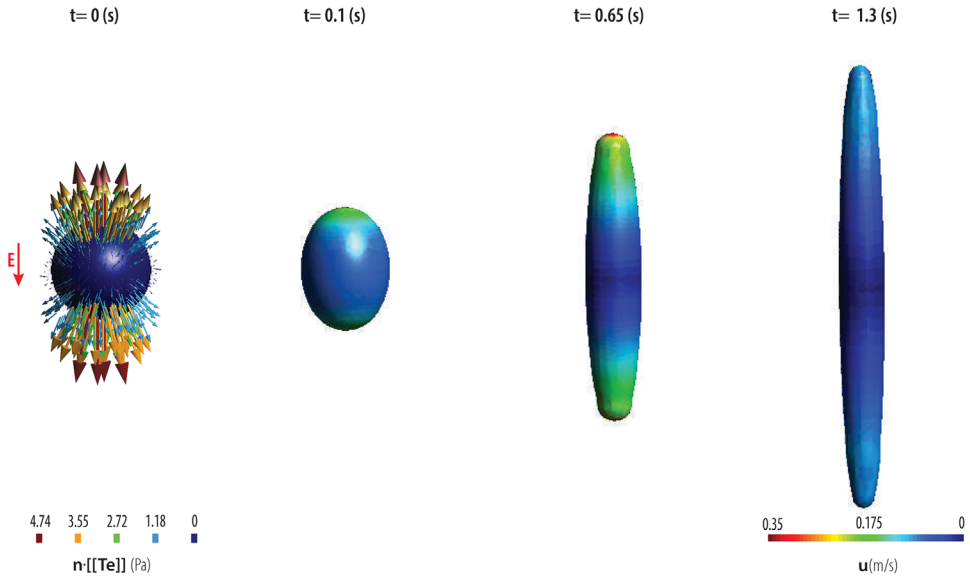

FIG. 11. Sequence of snapshots showing the elongation of droplet for $R = 10$.

In order to further investigate the effect of the wall, in Fig. 14, the pressure and magnitude of the velocity along the principal axes [see insets of Figs. 14(a)–14(c)] of the droplet are shown for three time instances $t = 0.01$, $t = 0.65$, and $t = 1.3$ s.

Upon the effect of the electric field, at the initial stage ($t = 0.1$ s), following the pulling of the tips, droplet experiences a circumferential shrinkage. Due to the constraint imposed by the no-slip wall on the surrounding medium, a suction toward the wall is produced in z-direction. This is evidenced by a large negative pressure in the proximity of the wall, i.e., at z close to 0 [see Fig. 14(a)]. This justifies the bulk movement of the entire droplet toward the wall, leading to reduction of the gap between the droplet and the wall. At later instances, as the rate of circumferential deformation becomes less significant [see Fig. 14(d)], the suction is also relaxed. The pressure difference on both sides of the droplet (next to the wall and the reciprocal side) is the reason for the creation of a "hump," observed in Figs. 13(j)–13(l).

In y-direction (which coincides with the direction of the externally applied electric field), in the first instance one can observe a large pressure drop inside the droplet and a significant pressure increment outside the droplet adjacent to the droplet surface [see Fig. 14(b)]. This occurs due to the large value of electric force, which is not counterbalanced at the beginning of the simulation, when the droplet is nearly undeformed. This effect becomes less significant as the time evolves, since the surface tension eventually counter-balances the electric force. This corresponds to a very large curvature value at the tips of the deformed droplet [see Figs. 13(d), 13(h), and 13(l)]. It can be noted that droplet deforms predominantly in the y-direction (i.e., tips move toward the electrodes) following the direction of the imposed electric field.

The fact that the electric force acts only at the interface is also reflected in the velocity graphs, where large velocities are observed at the tips, while at the barycenter of the droplet, the velocity is negligible. Note that the magnitude of the velocity decreases from step

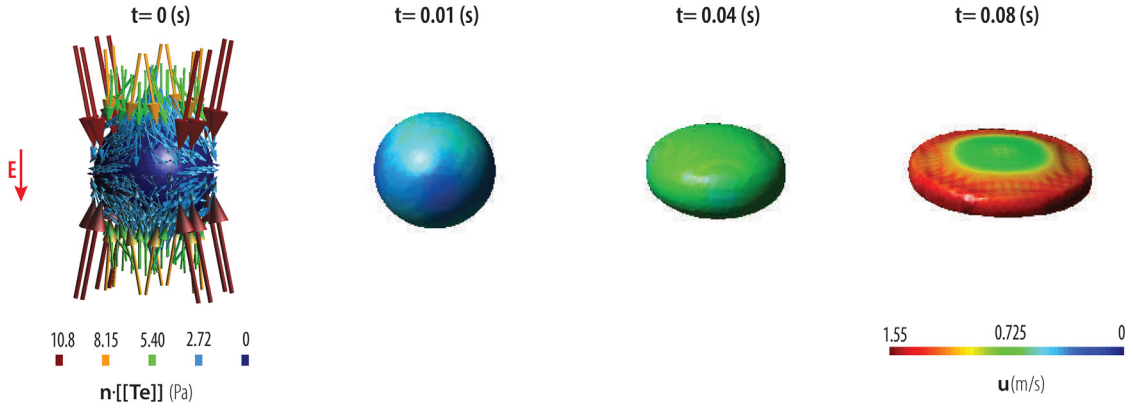

FIG. 12. Sequence of snapshots showing the elongation of droplet for $R = 0.1$.

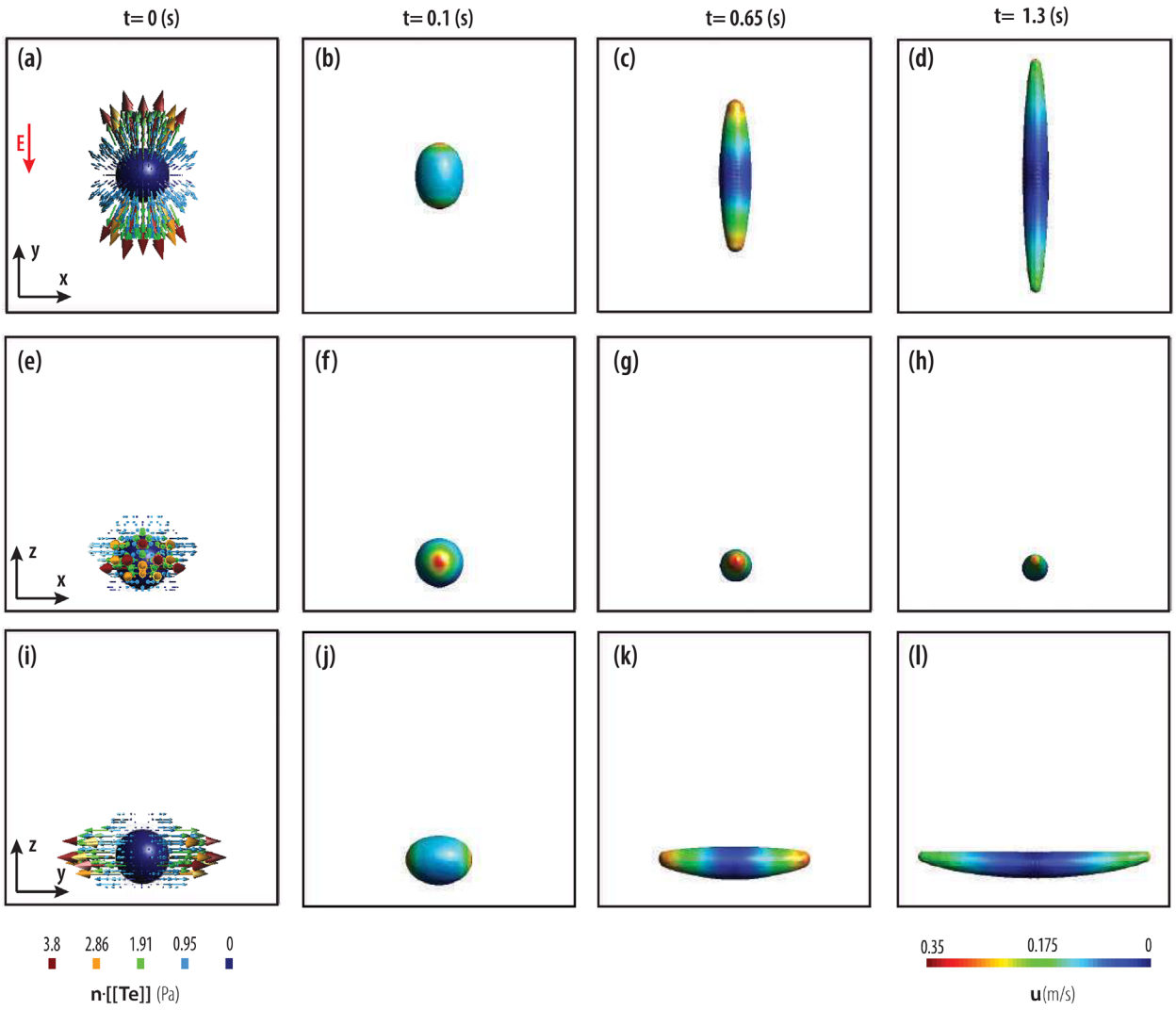

FIG. 13. Sequence of snapshots showing the nonsymetric deformation. The electric forces that act on the droplet are displayed in the first column. The four columns show the deformation at time instance, 0, 0.1, 0.65, and 1.3 s, respectively. (a)–(d) the evolution of deformation in *x*–*y* plane. (e)–(h) the evolution of deformation in *x*–*z* plane. (i) and (l) the evolution of deformation in *y*–*z* plane.

$t = 0.65(s)$ to $t = 1.3(s)$ as electric force, pressure, and surface tension tend to reach equilibrium.

Ultimately, in x-direction, as shown in Fig. 14(c), variation of the pressure inside the droplet is relatively small as the electric field is perpendicular to this direction. Thereby, the jump in the pressure is predominantly caused by surface tension.

The above-mentioned observations confirm that adjusting the proximity of the droplet to one of the walls influences the balance of the dominant forces and can be considered a means for controlling the droplet deformation. Similar observations have been reported in the literature.[52,57] Establishing quantitative correlation between the initial geometrical configuration (particularly, distance-to-the-walls) and the shape of the deformed droplet can be a basis for adaptation of droplets to the desired predefined shapes, which may be useful for microfluidic-based manufacturing, where specific morphology is sought for.

IV. CONCLUSIONS

A numerical model for electrohydrodynamics (EHD) is introduced within the framework of the Enriched Finite Element Method (EFEM). To the best of authors' knowledge, this is the first attempt of developing an EFEM formulation for the EHD flows. The main advantage of the proposed approach is the sharp (zero-thickness) treatment of the phase interface in both the electric and hydrodynamic problems. This leads to the realistic (physically consistent) modeling of the jump in the Maxwell stress (due to different electric material properties) as well as the pressure discontinuity (due to the surface tension).

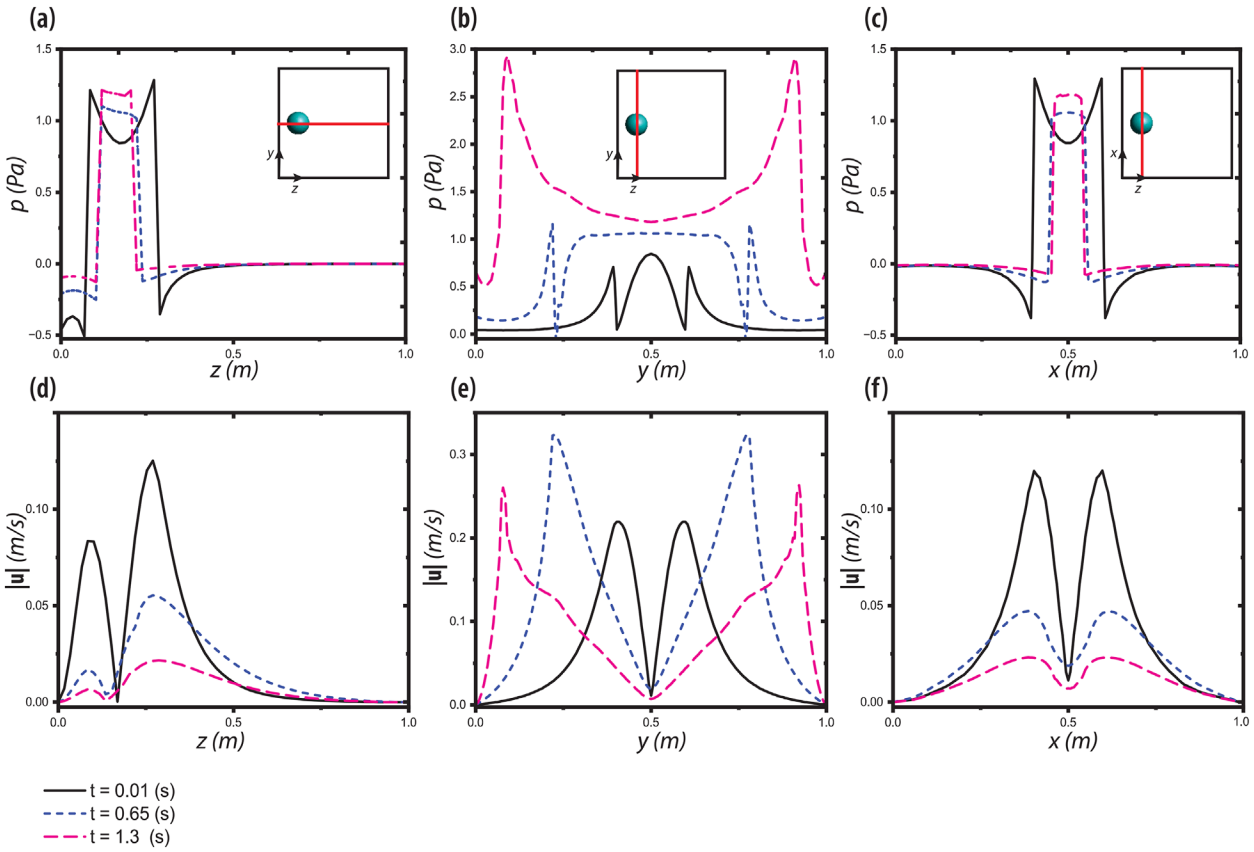

FIG. 14. Pressure and magnitude of velocity along the principal axes for three time instances $t = 0.01$, $t = 0.65$, and $t = 1.3$ s. (a) and (d) the pressure and magnitude of velocity along the z direction. (b) and (e) the pressure and magnitude of velocity along the y direction. (c) and (f) the pressure and magnitude of velocity along the x direction.

A series of two- and three-dimensional benchmark tests involving fluids with different permittivity and conductivity ratios were simulated. The results of the numerical simulations were compared with those obtained by a small deformation theory. The introduced method was further validated against the results of other numerical methods reported in the literature. In all test-cases, the results are in good agreement with the reference solutions. Comparing to the conventional smeared interface approaches, it is revealed that the proposed method provides more accurate results on coarser meshes. This, as the direct outcome of the realistic discontinuity treatment, leads to a significant improvement in the performance in the context of the numerical modeling of EHD problems, particularly important for cases where three-dimensional simulations are mandatory. Simulation of the spherical droplet exposed to an electric field in 3D revealed various deformation modes (straight stretching, curved stretching, and compression into a disk-like shape) depending on the conductivity ratio of the two fluids and initial conditions. The proposed model is particularly advantageous for problems, where symmetry of revolution cannot be ensured and, thus, where intrinsically 3D phenomena are expected. The approach can be applied for efficient fundamental analysis of EHD phenomena in problems where electrical stresses and wall-induced effects play an essential role. This can be used as a basis for establishing mechanisms of droplet shape control.

ACKNOWLEDGMENTS

The authors acknowledge the financial support of the Ministerio de Ciencia, Innovación e Universidades of Spain via the "Severo Ochoa Programme" for Centres of Excellence in R&D (Referece No. CEX2018-000797-S) given to the International Centre for Numerical Methods in Engineering (CIMNE). The work of C. Narvaez-Muñoz was supported by the "Severo Ochoa Ph.D. Scholarship" Reference No. PRE2020-096632. Parts of this work were done in the framework of DIDRO project (Toward establishing a Digital twin for manufacturing via drop-on-demand inkjet printing. Proyectos Estratégicos Orientados a la Transición Ecológica y a la Transición Digital. Reference No. TED2921-130471B-I00) supported by the Ministerio de Ciencia, Innovación e Universidades of Spain. M. Hashemi acknowledges the funding received from European Union's Horizon 2020 Research and Innovation Programme (European High-Performance Computing Joint Undertaking Grant Agreement No. 955558) as part of EFLOWS4HPC project. P. Ryzhakov and J. Pons-Prats are Serra Hunter fellows.

AUTHOR DECLARATIONS

Conflict of Interest

The authors have no conflicts to disclose.

Author Contributions

Christian Narváez-Muñoz: Conceptualization (equal); Formal analysis (equal); Validation (equal); Writing – original draft (equal); Writing – review & editing (equal). **Mohammad Reza Hashemi:** Conceptualization (equal); Formal analysis (equal); Writing – original draft (equal); Writing – review & editing (equal). **Pavel B. Ryzhakov:** Conceptualization (equal); Formal analysis (equal); Methodology (equal); Supervision (equal); Writing – review & editing (equal). **Jordi Pons-Prats:** Methodology (equal); Supervision (equal); Validation (equal); Writing – review & editing (equal).

DATA AVAILABILITY

The data that support the findings of this study are available from the corresponding authors upon reasonable request.

REFERENCES

[1]E. D. Fylladitakis, M. P. Theodoridis, and A. X. Moronis, "Review on the history, research, and applications of electrohydrodynamics," IEEE Trans. Plasma Sci. **42**, 358–375 (2014).

[2]L. J. Segura, C. N. Muñoz, C. Zhou, and H. Sun, "Sketch-based tensor decomposition for non-parametric monitoring of electrospinning processes," in *International Manufacturing Science and Engineering Conference* (American Society of Mechanical Engineers, 2020), Vol. 84263.

[3]Z. Jiang, Y. Gan, and Y. Luo, "Effect of viscosity ratio on the dynamic response of droplet deformation under a steady electric field," Phys. Fluids **32**, 053301 (2020).

[4]Y. Guan, S. Wu, M. Wang, Y. Tian, W. Lai, and Y. Huang, "Numerical analysis of electrohydrodynamic jet printing under constant and step change of electric voltages," Phys. Fluids **34**, 062005 (2022).

[5]H. J. Kwon, J. Hong, S. Y. Nam, H. H. Choi, X. Li, Y. J. Jeong, and S. H. Kim, "Overview of recent progress in electrohydrodynamic jet printing in practical printed electronics: Focus on variety of printable materials for each component," Mater. Adv. **2**, 5593–5615 (2021).

[6]D. Gao and J. Zhou, "Designs and applications of electrohydrodynamic 3D printing," Int. J. Bioprint. **5**, 172 (2018).

[7]C. P. Narvaez-Muñoz, L. M. Carrion-Matamoros, K. Vizuete, A. Debut, C. R. Arroyo, V. Guerrero, C. E. Almeida-Naranjo, V. Morales-Flórez, D. J. Mowbray, and C. Zamora-Ledezma, "Tailoring organic–organic poly (vinylpyrrolidone) microparticles and fibers with multiwalled carbon nanotubes for reinforced composites," ACS Appl. Nano Mater. **2**, 4302–4312 (2019).

[8]B. P. Van Poppel, O. Desjardins, and J. W. Daily, "A ghost fluid, level set methodology for simulating multiphase electrohydrodynamic flows with application to liquid fuel injection," J. Comput. Phys. **229**, 7977–7996 (2010).

[9]J.-J. Xu, W. Shi, W.-F. Hu, and J.-J. Huang, "A level-set immersed interface method for simulating the electrohydrodynamics," J. Comput. Phys. **400**, 108956 (2020).

[10]P. S. Casas, M. Garzon, L. J. Gray, and J. A. Sethian, "Numerical study on electrohydrodynamic multiple droplet interactions," Phys. Rev. E **100**, 063111 (2019).

[11]K. E. Teigen and S. T. Munkejord, "Sharp-interface simulations of drop deformation in electric fields," IEEE Trans. Dielectr. Electr. Insul. **16**, 475–482 (2009).

[12]M. R. Hashemi, P. B. Ryzhakov, and R. Rossi, "Toward droplet dynamics simulation in polymer electrolyte membrane fuel cells: Three-dimensional numerical modeling of confined water droplets with dynamic contact angle and hysteresis," Phys. Fluids **33**, 122109 (2021).

[13]G. Tomar, D. Gerlach, G. Biswas, N. Alleborn, A. Sharma, F. Durst, S. W. J. Welch, and A. Delgado, "Two-phase electrohydrodynamic simulations using a volume-of-fluid approach," J. Comput. Phys. **227**, 1267–1285 (2007).

[14]J. M. López-Herrera, S. Popinet, and M. A. Herrada, "A charge-conservative approach for simulating electrohydrodynamic two-phase flows using volume-of-fluid," J. Comput. Phys. **230**, 1939–1955 (2011).

[15]C. Narváez-Muñoz, P. Ryzhakov, and J. Pons-Prats, "Determination of the operational parameters for the manufacturing of spherical PVP particles via electrospray," Polymers **13**, 529 (2021).

[16]A. Panahi, A. R. Pishevar, and M. R. Tavakoli, "Experimental investigation of electrohydrodynamic modes in electrospraying of viscoelastic polymeric solutions," Phys. Fluids **32**, 012116 (2020).

[17]X. Zhao, D. Wang, Y. Lin, Y. Sun, T. Ren, J. Liang, and M. Madou, "Numerical simulation of coaxial electrohydrodynamic jet and printing nanoscale structures," Microsyst. Technol. **25**, 4651–4661 (2019).

[18]J. Zhang and D. Y. Kwok, "A 2D lattice Boltzmann study on electrohydrodynamic drop deformation with the leaky dielectric theory," J. Comput. Phys. **206**, 150–161 (2005).

[19]L. Wang, Z. Wei, T. Li, Z. Chai, and B. Shi, "A lattice Boltzmann modelling of electrohydrodynamic conduction phenomenon in dielectric liquids," Appl. Math. Modell. **95**, 361–378 (2021).

[20]A. Rahmat, N. Tofighi, and M. Yildiz, "Numerical simulation of the electrohydrodynamic effects on bubble rising using the SPH method," Int. J. Heat Fluid Flow **62**, 313–323 (2016).

[21]F. Almasi, M. S. Shadloo, A. Hadjadj, M. Ozbulut, N. Tofighi, and M. Yildiz, "Numerical simulations of multi-phase electro-hydrodynamics flows using a simple incompressible smoothed particle hydrodynamics method," Comput. Math. Appl. **81**, 772–785 (2021).

[22]W.-F. Hu, M.-C. Lai, and Y.-N. Young, "A hybrid immersed boundary and immersed interface method for electrohydrodynamic simulations," J. Comput. Phys. **282**, 47–61 (2015).

[23]P. B. Ryzhakov and A. Jarauta, "An embedded approach for immiscible multi-fluid problems," Int. J. Numer. Methods Fluids **81**, 357–376 (2016).

[24]A. Jarauta, P. Ryzhakov, M. Secanell, P. R. Waghmare, and J. Pons-Prats, "Numerical study of droplet dynamics in a polymer electrolyte fuel cell gas channel using an embedded Eulerian-Lagrangian approach," J. Power Sources **323**, 201–212 (2016).

[25]S. Idelsohn, M. Mier-Torrecilla, and E. Oñate, "Multi-fluid flows with the particle finite element method," Comput. Methods Appl. Mech. Eng. **198**, 2750–2767 (2009).

[26]P. B. Ryzhakov, A. Jarauta, M. Secanell, and J. Pons-Prats, "On the application of the PFEM to droplet dynamics modeling in fuel cells," Comput. Part. Mech. **4**, 285–295 (2017).

[27]K. Adamiak, "Interaction of two dielectric or conducting droplets aligned in the uniform electric field," J. Electrost. **51–52**, 578–584 (2001).

[28]H. Dastourani, M. R. Jahannama, and A. Eslami-Majd, "A physical insight into electrospray process in cone-jet mode: Role of operating parameters," Int. J. Heat Fluid Flow **70**, 315–335 (2018).

[29]C. Rinaldi and H. Brenner, "Body versus surface forces in continuum mechanics: Is the maxwell stress tensor a physically objective Cauchy stress," Phys. Rev. E **65**, 036615 (2002).

[30]C.-H. Chen, "Electrohydrodynamic stability," in *Electrokinetics and Electrohydrodynamics in Microsystems* (Springer, 2011), pp. 177–220.

[31]J. R. Melcher and G. I. Taylor, "Electrohydrodynamics: A review of the role of interfacial shear stresses," Annu. Rev. Fluid Mech. **1**, 111–146 (1969).

[32]J. R. Melcher, *Continuum Electromechanics* (MIT Press, Cambridge, MA, 1981), Vol. 2.

[33]S. Osher and R. P. Fedkiw, "Level set methods: An overview and some recent results," J. Comput. Phys. **169**, 463–502 (2001).

[34]R. F. Ausas, G. C. Buscaglia, and S. R. Idelsohn, "A new enrichment space for the treatment of discontinuous pressures in multi-fluid flows," Int. J. Numer. Methods Fluids **70**, 829–850 (2012).

[35]S. R. Idelsohn, J. M. Gimenez, J. Marti, and N. M. Nigro, "Elemental enriched spaces for the treatment of weak and strong discontinuous fields," Comput. Methods Appl. Mech. Eng. **313**, 535–559 (2017).

[36]C. Narváez-Muñoz, M. R. Hashemi, P. Ryzhakov, J. Pons-Prats, and H. Owen, "Enriched finite element formulation for discontinuous electric field in electrohydrodynamic problems," in *XIV Iberian Meeting on Computational Electromagnetics* (Universitat Politècnica de Catalunya, 2022).

[37]D. A. Saville, "Electrohydrodynamics: The Taylor-Melcher leaky dielectric model," Annu. Rev. Fluid Mech. **29**, 27–64 (1997).

[38]J. Q. Feng and T. C. Scott, "A computational analysis of electrohydrodynamics of a leaky dielectric drop in an electric field," J. Fluid Mech. **311**, 289–326 (1996).
[39]M. R. Hashemi, P. B. Ryzhakov, and R. Rossi, "An enriched finite element/level-set method for simulating two-phase incompressible fluid flows with surface tension," Comput. Methods Appl. Mech. Eng. **370**, 113277 (2020).
[40]C. Narváez-Muñoz, M. R. Hashemi, P. B. Ryzhakov, J. Pons-Prats, and H. Owens, "Enriched finite element approach for modeling discontinuous electric field in multimaterial problems," Comput. Methods Appl. Mech. Eng. arXiv preprint arXiv:2212.0854 (2022).
[41]R. Rossi, "An object-oriented environment for developing finite element codes for multi-disciplinary applications," Arch. Comput. Methods Eng. **17**(3), 253–297 (2010); available at https://www.academia.edu/19923275/An_Object_oriented_Environment_for_Developing_Finite_Element_Codes_for_Multi_disciplinary_Applications.
[42]P. Dadvand, R. Rossi, and E. Oñate, "An object-oriented environment for developing finite element codes for multi-disciplinary applications," Arch. Comput. Methods Eng. **17**, 253–297 (2010).
[43]M. N. Reddy and A. Esmaeeli, "The EHD-driven fluid flow and deformation of a liquid jet by a transverse electric field," Int. J. Multiphase Flow **35**, 1051–1065 (2009).
[44]H. Paknemat, A. R. Pishevar, and P. Pournaderi, "Numerical simulation of drop deformations and breakup modes caused by direct current electric fields," Phys. Fluids **24**, 102101 (2012).
[45]J.-W. Ha and S.-M. Yang, "Deformation and breakup of Newtonian and non-Newtonian conducting drops in an electric field," J. Fluid Mech. **405**, 131–156 (2000).
[46]J. Q. Feng, "A 2D electrohydrodynamic model for electrorotation of fluid drops," J. Colloid Interface Sci. **246**, 112–121 (2002).
[47]K. Luo, J. Wu, H.-L. Yi, and H.-P. Tan, "Numerical analysis of two-phase electrohydrodynamic flows in the presence of surface charge convection," Phys. Fluids **32**, 123606 (2020).
[48]Y. Cui, N. Wang, and H. Liu, "Numerical study of droplet dynamics in a steady electric field using a hybrid lattice Boltzmann and finite volume method," Phys. Fluids **31**, 022105 (2019).
[49]X. Liu, Z. Chai, and B. Shi, "A phase-field-based lattice Boltzmann modeling of two-phase electro-hydrodynamic flows," Phys. Fluids **31**, 092103 (2019).
[50]N. C. Lima and M. A. d'Avila, "Numerical simulation of electrohydrodynamic flows of newtonian and viscoelastic droplets," J. Non-Newtonian Fluid Mech. **213**, 1–14 (2014).
[51]I. Roghair, M. Musterd, D. van den Ende, C. Kleijn, M. Kreutzer, and F. Mugele, "A numerical technique to simulate display pixels based on electrowetting," Microfluid. Nanofluid. **19**, 465–482 (2015).
[52]R. Saghatchi, A. Rahmat, and M. Yildiz, "Electrohydrodynamics of a droplet in a highly confined domain: A numerical study," Phys. Fluids **32**, 123305 (2020).
[53]G. I. Taylor, "Studies in electrohydrodynamics. I. The circulation produced in a drop by an electric field," Proc. R. Soc. London, Ser. A **291**, 159–166 (1966).
[54]O. O. Ajayi, "A note on Taylor's electrohydrodynamic theory," Proc. R. Soc. London, Ser. A **364**, 499–507 (1978).
[55]C. Narvaez-Munoz, *Computational Modelling of Electrohydrodynamic Atomization* (The University of Manchester, United Kingdom, 2014).
[56]O. Ghazian, K. Adamiak, and G. S. P. Castle, "Numerical simulation of electrically deformed droplets less conductive than ambient fluid," Colloids Surf., A **423**, 27–34 (2013).
[57]S. Santra, S. Mandal, and S. Chakraborty, "Electrohydrodynamics of confined two-dimensional liquid droplets in uniform electric field," Phys. Fluids **30**, 062003 (2018).